

Reports

Laboratory Experiments on Planetary and Stellar Convection Performed on Spacelab 3

J. E. HART, J. TOOMRE, A. E. DEANE, N. E. HURLBURT,
G. A. GLATZMAIER, G. H. FICHTL, F. LESLIE, W. W. FOWLIS,
P. A. GILMAN

Experiments on thermal convection in a rotating, differentially heated hemispherical shell with a radial buoyancy force were conducted in an orbiting microgravity laboratory. A variety of convective structures, or planforms, were observed, depending on the magnitude of the rotation and the nature of the imposed heating distribution. The results are compared with numerical simulations that can be conducted at the more modest heating rates, and suggest possible regimes of motion in rotating planets and stars.

LARGE-SCALE ATMOSPHERIC MOTIONS on rotating planets and stars are influenced by both buoyancy and Coriolis forces. On a spherical surface the Coriolis force varies with latitude, and this variation is thought to be a fundamental influence in a wide range of phenomena of interest to geophysicists and astrophysicists. These phenomena include cloud-band orientation in planetary atmospheres, differential rotation in the solar atmosphere, the formation of jet streams, and magnetic dynamo action. Except for flows of a uniform fluid, so that buoyancy-driven motions are absent, it has been difficult to properly model global motions of spherically contained rotating fluids in the terrestrial laboratory. When the rotation vector Ω is inclined to earth's gravity \mathbf{g} , an oscillatory body force results that has no geophysical analog. Therefore, previous laboratory experiments on thermally driven global circulations have been confined either to (i) studies of convection near the poles where Ω and \mathbf{g} are nearly parallel and the geometry is effectively flat (1), or (ii) studies of motions close to the equator where Ω and \mathbf{g} are nearly perpendicular, with the effects of gravity being simulated by centrifugal buoyancy forces associated with very rapid rotation (2).

Our laboratory model, which consistently simulates large-scale convective motions in a full hemispherical shell of incompressible fluid, is based on the existence of density-dependent electrostatic forces in a dielectric medium. Because these forces are relatively weak, it is necessary to conduct the experiment in an environment where \mathbf{g} is small. This report describes our instrument, the Geophysical Fluid Flow Cell, and gives a preliminary description of results from experiments carried out aboard the Spacelab 3

microgravity laboratory that flew on the space shuttle Challenger in May 1985.

The motion of an incompressible fluid is entirely governed by the vorticity equation, obtained by taking the curl of the momentum equations. In a dielectric liquid subject to imposed electric field gradients, polarization forces will be present in addition to normal buoyancy. The nonconservative part of these forces contributes to vorticity generation. As shown in (3), this generation is proportional to

$$\text{curl (body force)} = \alpha \nabla T \times \nabla \Phi + 1/2 \epsilon \gamma \nabla T \times \nabla |\mathbf{E}|^2 \quad (1)$$

where α is the thermal expansivity, T is the temperature, Φ is the geopotential, \mathbf{E} is the electric field, ϵ is the average dielectric constant of the liquid, and γ is the temperature coefficient of the dielectric constant. In a self-gravitating fluid Φ is an inverse function of radius r . We would like the first and second terms on the right side of Eq. 1 to be isomorphic functions. A simulation of thermal buoyancy in a radial geopotential may be attained when an electric field $\mathbf{E} \approx r^{-2} \hat{\mathbf{r}}$ is generated in the liquid by applying a uniform electric potential across two concentric spherical surfaces. The resulting electrostatic "gravity," which is proportional to $\nabla |\mathbf{E}|^2$, varies like r^{-5} instead of r^{-2} , as might be desired, but it has been shown theoretically that the unstable eigenfunctions and other properties of thermal convection in a nonrotating spherical shell containing a Boussinesq liquid (nearly incompressible) are essentially unaffected by this difference (4). The magnitude of the electrostatic "gravity" is limited by the breakdown field strength of existing low-viscosity, low-loss dielectrics to about $0.1 g$ (or 1 m sec^{-2}) in an apparatus of reasonable size. Thus the use of electrodynamic forces to study convection in spheri-

cal shells is only practical in the microgravity environment of the shuttle orbiter.

A diagram of the cell used in our experiment is shown in Fig. 1. A dielectric silicone oil of 0.65-centistoke viscosity is contained between two hemispherical shells that form part of a spherical capacitor. We study fluid motions in a single hemisphere because non-radial electric fields occur in the vicinity of the inner sphere's mechanical support which spans the annular gap near the south pole. The inner shell at radius R_i is made of polished nickel, and the outer at radius R_o is a transparent sapphire dome about 1 cm thick. Temperatures are maintained along both these surfaces by a system of heater coils and thermistor sensors installed in a computer-controlled servo loop. The thermal boundary conditions are axisymmetric but allow for variations of both inner (T_i) and outer (T_o) surface temperature with latitude θ . Although uniform differential heating, with $T_i > T_o$ and independent of θ , is the simplest and most relevant case for modeling objects with spherically symmetric forcing, several experiments were run with a hotter pole. Such statically unstable, non-uniform heating is thought to occur in rapidly rotating stars, giving rise to a meridional circulation (5) with little-known non-axisymmetric instability properties. Theoretical studies have shown that the spatial patterns or planforms selected by global convective modes can be influenced by latitudinal gradients in the applied heating, and that this selection may be related to the structure of Jovian cloud bands (6).

To generate the electrostatic gravity, a 300-Hz alternating potential V_o is applied to a transparent conducting coating on the inner wall of the outer hemisphere. The inner sphere is grounded. The field reverses in a period short by comparison to the charge relaxation time for the fluid. This ensures an absence of electric currents and associated nongeophysical instabilities. In addition, the oil has such a low dielectric loss that internal dissipative heating, even with potentials as high as 10 kV, is entirely negligible. The cell assembly, including the high-voltage supply and the thermal-control circuitry, is mounted on a rotating turntable that maintains a constant but adjustable rotation rate Ω . At its most rapid rotation, the turntable makes one revolution in 2 seconds; faster rates are not chosen to ensure

J. E. Hart, J. Toomre, A. E. Deane, N. E. Hurlburt, Department of Astrophysical, Planetary, and Atmospheric Sciences and Joint Institute for Laboratory Astrophysics, University of Colorado, Boulder, CO 80309.
G. A. Glatzmaier, Los Alamos National Laboratory, Los Alamos, NM 87545.
G. H. Fichtl, F. Leslie, W. W. Fowles, NASA Marshall Space Flight Center, Huntsville, AL 35812.
P. A. Gilman, High Altitude Observatory, National Center for Atmospheric Research, Boulder, CO 80307.

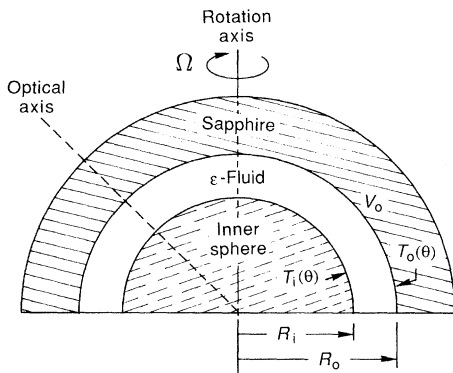


Fig. 1. Cross section of the experimental cell used to study thermal convection under the effects of rotation Ω in a hemispherical shell of fluid in the presence of an electrical analog of a radial gravity field. The inner radius of the shell of fluid is $R_i = 2.402$ cm and the outer radius $R_o = 3.300$ cm. The electrostatic gravity is achieved by imposing an alternating electrical potential V_o across the fluid shell. The dielectric silicone working fluid is bounded on the outside by a transparent sapphire dome to allow optical probing of the convective flows and thermal structures that result from differential heating.

that centrifugal forces are negligible compared to buoyancy forces associated with the electrostatic gravity. During the actual mission, rotation rates were held constant to better than 0.5% over a typical fluid overturning time (~ 50 seconds). The applied high voltage remained within a similar bound. The imposed temperatures on the inner and outer surfaces were held constant in time within about 0.1°C , compared to a typical imposed radial temperature difference across the fluid shell of 10°C . The failure of a heater loop at the inner equator limited the latitudinal gradients that could be imposed on T_i near the equator. However, the temperature sensors at all times allowed us to determine the profiles $T_i(\theta)$ and $T_o(\theta)$ that were attained.

Flows are visualized by Schlieren and shadowgraph photography. A nonrotating optical train focuses light from a grating onto the inner sphere. Thermally induced variations in the refractive index of the fluid cause individual rays to bend. When the incident rays are compared with the reflected rays, various measures of the radially averaged temperature field in the fluid are obtained. Because of space and weight limitations, the optical system does not image the whole hemisphere; rather, a circular view extending from equator to pole and covering a quadrant in longitude is obtained. The mapping, as indicated in Fig. 2, is moderately nonlinear. Some lines at constant latitude are scored on the outer hemisphere and appear as light circles on the images. The 30° latitude line is emphasized in Fig. 3b. The length of this latitude line from edge to edge, as seen in the image,

spans a distance equal to 110° in longitude or $5.22 \times D$, where $D = 0.908$ cm is the fluid layer depth. This latter measure is useful in estimating the characteristic horizontal scales of the convection. The experiments yielded over 50,000 images during the 110 hours of operation of the apparatus.

There are several nondimensional numbers that serve to define the convective flow regimes. The fixed parameters are the Prandtl number $Pr = (\text{viscosity } \nu)/(\text{thermal diffusivity } \kappa) = 8.4$ and the aspect ratio $R_i/R_o = 2.402 \text{ cm}/3.300 \text{ cm} = 0.73$. The measure of rotation is taken to be the Taylor number

$$Ta = \frac{4\Omega^2(R_o - R_i)^4}{\nu^2} \quad (2)$$

For the most rapid rotation of the turntable (period of 2 seconds), $Ta = 6.1 \times 10^5$. The Rayleigh number indicates the degree of thermal forcing with respect to dissipation. It is defined by

$$Ra = g_o \frac{\gamma \Delta T_r (R_o - R_i)^3}{\nu \kappa} \quad (3)$$

where g_o is the equivalent electrostatic gravity at $r = R_o$ and $\Delta T_r \equiv T_i - T_o$ is the radial temperature difference across the fluid at the equator. Finally, $H \equiv \Delta T_\theta / \Delta T_r$ compares the imposed pole-to-equator temperature difference at the boundaries to the radial temperature difference (with H vanishing for uniform heating).

A sequence of Schlieren images for cases with uniform imposed temperature on each hemisphere ($H \approx 0$) is shown in Fig. 3. In Fig. 3a Ta is relatively small and rotational effects are weak. At a Ra above about 2×10^3 , convective instabilities form and break the spherical symmetry of the conductive thermal balance that exists at smaller Ra . The tessellated pattern shows little influence of rotation and evolves slowly with time. The patterns are suggestive of those predicted by a theory (7) for planform selection in a nonrotating shell without the rigid equatorial boundary. The observed convection has narrow updrafts along the edges of the cells and broad sinking regions in cell centers. One possible explanation is that this is a result of radial asymmetry in the "gravity" that is concentrated near the inner sphere. For example, it has been shown (8) that planar convection in a layer with unstable thermal gradients concentrated near the lower wall is dominated by hexagons with downflow in the center and upflow at the edges. Another explanation, suggested by similar results from our numerical simulations of flows with either r^{-2} or r^{-5} gravity, is that the narrow updrafts are a result of strong nonlinear interactions in the spherical geometry.

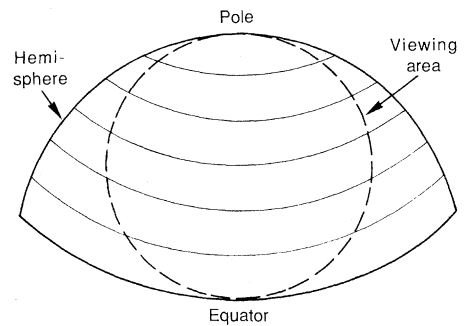


Fig. 2. Sketch of the Schlieren viewing configuration with respect to the hemispherical shell.

As Ra is increased, with Ta held constant at this low value, the scales of the convection cells shrink and their boundaries become sharper with highly concentrated thermal gradients at the cell edges (Fig. 3b). The flow becomes more strongly time-dependent as Ra becomes larger. For example, the image in Fig. 3c illustrates one instantaneous view of a highly turbulent flow. These cases with low Ta and with spherically symmetric heating are horizontally isotropic, showing no evidence for preferred cell alignments or systematic pattern propagation in longitude.

As Ta is increased, the influence of rotation becomes larger (Fig. 4a). The weakly supercritical convective modes begin to feel the Taylor-Proudman constraint (9) that the motion should be invariant in the direction of Ω . In agreement with earlier analytical and numerical calculations (10), the boundaries of the convection cells are aligned in the north-south direction. The convection dies out somewhat north of the critical latitude (11) on the outer boundary, here 43° , where a tangent cylinder drawn parallel to Ω just intersects the inner sphere at the equator. These low-latitude "banana cells" have a prograde propagation, which is revealed in extended sequences of shadowgraph images. The banana cells dominate the weakly unstable flows (that is, modest Ra) at all Ta greater than about 10^4 . However, as Ra is increased, mid-latitude and polar modes become unstable as well. In Fig. 4b, interactions with retrograde-propagating mid-latitude convection modes occur at the tips of the banana cells. This causes a wavering and, at higher Ra , a nearly complete erosion of the banana cells. In Fig. 4c, vestiges of the Taylor-Proudman constraint are found only within 20° of the equator. The remaining convection is highly turbulent, more horizontally isotropic, and contains most of the root-mean-square temperature variance.

A series of experiments with $H \approx 1$ is illustrated in Fig. 5. Because the pole is hotter than the equator on each boundary,

there is no purely conductive motionless state. A meridional circulation always exists, and, with even a small amount of rotation, substantial zonal flows will be generated. The interaction of this axisymmetric motion with incipient nonaxisymmetric convective instabilities leads to the spiral pattern of convection at low T_a (Fig. 5a). The rolls tip west (to the right) as one follows an updraft equatorward. The updrafts are narrow and the downdrafts are broad. If R_a is increased at this T_a (Fig. 5b), the thermal fronts along the spiral wave boundaries sharpen and a secondary instability in the form of kinks occurs. The resulting defects lead to an irregular pattern that evolves chaotically in time. At even larger R_a (Fig. 5c), cross-branches form and the pattern becomes more cellular in character; the ratio of R_a to T_a is large and similar to that in Fig. 3c. Yet here the interaction of the rotationally influenced meridional circulation (generated by the applied latitudinal temperature gradient) with the convective instabilities leads to a preferred average alignment or tilt of the cell boundaries, much as occurs in the weakly unstable case (Fig. 5a).

Figure 6 shows some of the complex behavior that arises when moderate radial and strong north-south heating occur in concert with rapid rotation. At large T_a weak banana cells reappear in the equatorial regions. These columnar disturbances interact in varying degrees with different wavy structures at higher latitudes. At low R_a (Fig. 6a) quasi-axisymmetric bands occur near the pole. Retrograde-propagating waves appear on the bands. At high R_a (Fig. 6b), a complicated turbulent flow is observed. Yet imbedded in the circulation are fairly stable, triangularly shaped waves that appear to arise as a coupling between the polar disturbances and the low-latitude banana cells. When the latitudinal differential heating is made larger with respect to the imposed radial gradient (Fig. 6c), the flow stabilizes a bit, with preference for wavy spirals near the poles and a relative absence of equatorial banana cells.

Numerical solution of the governing Boussinesq hydrodynamic equations is practical with supercomputers for some of the cases with lower R_a that have been studied experimentally. Such simulations provide complementary tools in understanding the detailed dynamical interactions involved in pattern selection, secondary instabilities, and transitions to turbulence. We have solved the nonlinear three-dimensional problem in spherical geometry, using a spectral transform method (12). The velocity and thermodynamic functions are expanded in spherical harmonics in longitude and latitude, and Chebyshev polynomials in ra-

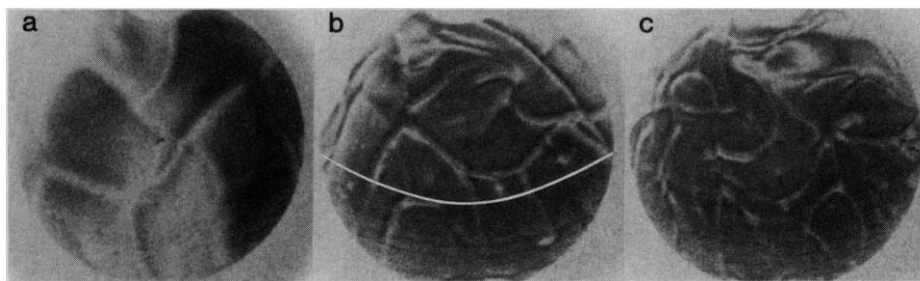


Fig. 3. Planforms for the convection as observed with Schlieren photography in experiments with a uniform radial temperature difference imposed between the inner and outer spheres ($H \approx 0$) and a weak rotational influence. The convection has a tessellated pattern with no preferred orientation, appearing at onset rather like a soccer ball. These circular views of a portion of the hemisphere extend from the pole at the top to the equator at the bottom, as indicated in Fig. 2. The 30° latitude line is delineated in (b). The basic rotation is from right (west) to left (east), and $T_a = 1.1 \times 10^3$. (a) $R_a = 1.0 \times 10^4$; (b) $R_a = 1.2 \times 10^5$; (c) $R_a = 2.5 \times 10^5$.

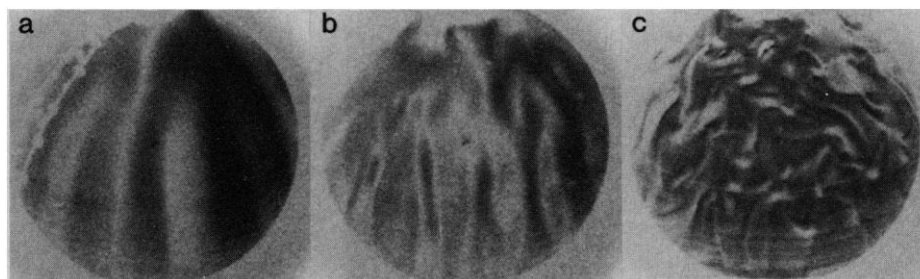


Fig. 4. Planforms for the convection as in Fig. 3 with $H \approx 0$, but rotational effects are emphasized, leading to convection in the form of banana cells aligned with the rotation axis. The temperature sensors in the outer sapphire dome cast the white lines seen to the left in (a). $R_a = 4.1 \times 10^3$, $T_a = 3.8 \times 10^4$; (b) $R_a = 7.9 \times 10^4$, $T_a = 6.1 \times 10^5$; (c) $R_a = 2.9 \times 10^5$, $T_a = 6.1 \times 10^5$.

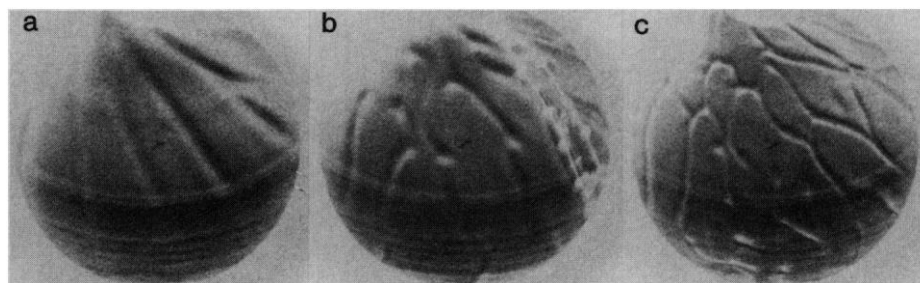


Fig. 5. Planforms for the convection observed in experiments with temperature increasing poleward on each spherical boundary in addition to a uniform radial temperature difference between the spheres ($H \approx 1$), with $T_a = 1.1 \times 10^3$. Even though the rotation is slow, the latitudinal temperature gradient and the resulting meridional circulation lead to convection cells with a distinctive east-west tilt. These spiral waves experience secondary instabilities that produce cross-branches. (a) $R_a = 1.7 \times 10^4$; (b) $R_a = 5.0 \times 10^4$; (c) $R_a = 1.9 \times 10^5$.

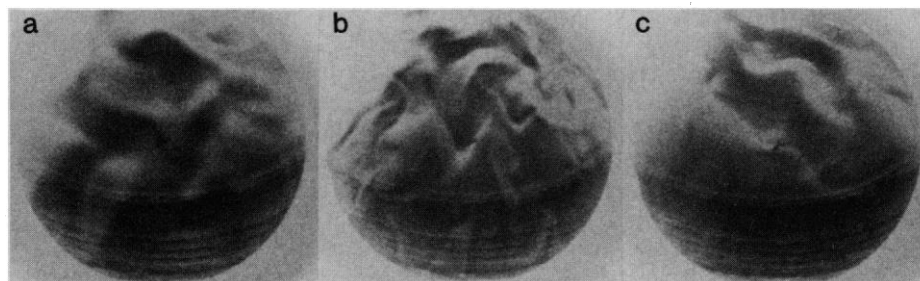


Fig. 6. Planforms for the convection as in Fig. 5, but rotation is more rapid. Wavy disturbances at high latitudes interact with banana cells at low latitudes. Unusual triangularly shaped waves are seen. (a) $R_a = 1.7 \times 10^4$, $T_a = 3.8 \times 10^4$, $H \approx 1$; (b) $R_a = 1.9 \times 10^5$, $T_a = 6.1 \times 10^5$, $H \approx 1$; (c) $R_a = 1.4 \times 10^5$, $T_a = 6.1 \times 10^5$, $H \approx 1.6$.

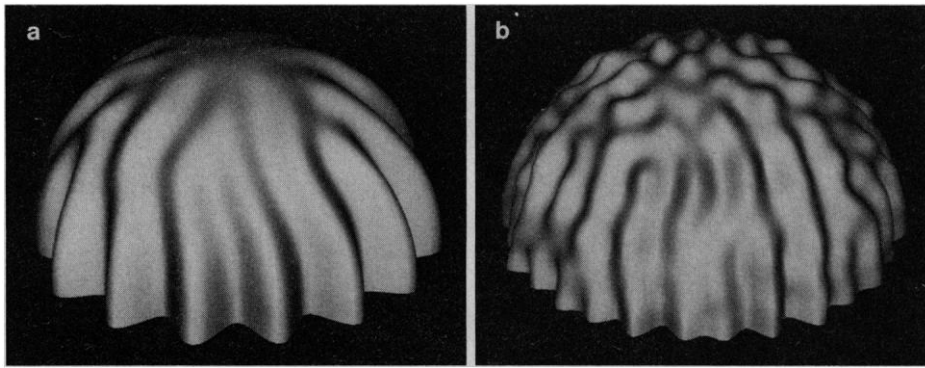


Fig. 7. Surface plots of computed radial velocity at mid-depth in a rotating hemispherical shell as obtained from three-dimensional numerical simulations. Elevation of the surface represents upflow, depression downflow: (a) for conditions corresponding to those in Fig. 4a and (b) for conditions corresponding to those in Fig. 4b.

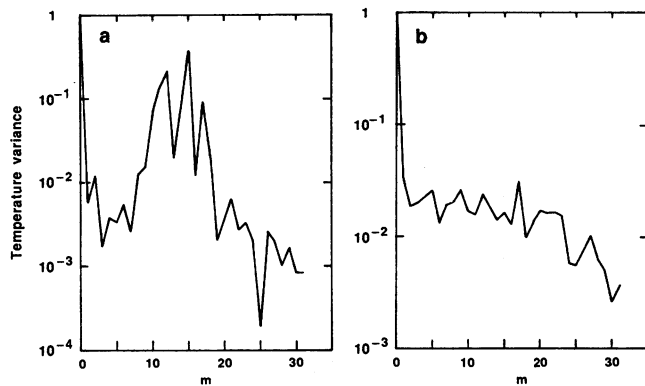


Fig. 8. Latitudinally and radially averaged root-mean-square temperature variance as a function of longitudinal wave number m for the numerically computed flows of (a) Fig. 7a and (b) Fig. 7b.

dius. All the conditions of the laboratory experiment are modeled except for the no-slip velocity constraint at the equatorial barrier, which is replaced by a stress-free condition. Computations carried out with the use of a slower finite-difference model, in which the proper equatorial condition can be implemented, indicate that it exerts no major influence on the fluid flow at latitudes more than a few degrees above the equatorial plane. Figure 7a shows the mid-depth radial velocity pattern, which is essentially the same as the radially averaged thermal pattern, for the conditions of Fig. 4a. These banana cells are very robust structures. The thermal spectrum peaks near wave number $m = 15$ (Fig. 8a). The experiment is also dominated by wave number 15. The banana cells seen in the simulation translate uniformly westward (retrograde) at a slow rate of $\approx 0.45^\circ$ per rotation. This propagation speed is weak compared to fluid parcel velocities in the convection. Further calculations have shown that the direction of propagation, in this parameter range, is sensitive to the presence of small latitudinal temperature gradients (for example, for $H = 0.2$, the computed pattern translates in a prograde direction). This sensitivity study gives a possible explanation for the discrepancy in the sense of propagation of the banana cells between computations with spherically sym-

metric boundary conditions and laboratory experiments that are unable to maintain such symmetries exactly.

The differential rotation produced in the numerical model is retrograde at the equator and contributes about 1% to the total kinetic energy. Our results agree with earlier predictions (13, 14) that both rigid boundary conditions and the relatively high Prandtl number tend to suppress differential rotation, when compared to the large zonally averaged flows predicted in models of solar convection with stress-free boundaries and a Prandtl number of unity (15). A numerical simulation of a rapidly rotating and more unstable case is shown in Fig. 7b for the same conditions as Fig. 4b. The calculated flow now includes a substantial contribution from polar and mid-latitude modes that are observed to interact with the tips of the banana cells, much as seen in the experiment. The thermal spectrum (Fig. 8b) is broad with a weak maximum at longitudinal wave number 17. The broad character of this spectrum is due in part to the latitudinal average that includes contributions from the very different structures at the pole. If only low latitudes are considered, the $m = 17$ peak is more prominent and compares favorably with the experimental value of 18 measured in this region. In this case the computed differential rotation is concentrated near

the poles with a structure that depends on the meridional circulation there. Typically there is downward flow at the pole with prograde differential rotation in the upper part of the fluid shell and retrograde differential rotation in the lower part.

The experiments have supplied new data on pattern selection and low- and mid-latitude interactions in rotating, thermally unstable flows (16). Physical interpretation of these results, and future experiments on secondary instability and the transition to turbulence, should provide new insights into nonlinear processes important in the dynamics of planetary and stellar convection.

REFERENCES AND NOTES

1. H. T. Rossby, *J. Fluid Mech.* **36**, 309 (1969).
2. F. H. Busse and C. R. Carrigan, *Science* **191**, 81 (1976); C. R. Carrigan and F. H. Busse, *J. Fluid Mech.* **126**, 287 (1983).
3. J. E. Hart, *NASA Rep. CR-2753* (1976). A general discussion of electrohydrodynamics has been provided by J. R. Melcher and G. I. Taylor [*Annu. Rev. Fluid Mech.* **1**, 111 (1969)]. An implementation of this concept in cylindrical geometry has been presented by B. Chandra and D. E. Smylie [*Geophys. Fluid Dyn.* **3**, 211 (1972)].
4. J. E. Hart and J. Toomre, *NASA Rep. NAS-8-31958* (1977) (available from the authors). For aspect ratios R_i/R_o , smaller than that used in our instrument the differences can become significant.
5. A. J. Eddington, *Observatory* **48**, 73 (1925); P. A. Sweet, *Mon. Not. R. Astron. Soc.* **110**, 548 (1950); J. L. Tassoul, *Theory of Rotating Stars* (Princeton Univ. Press, Princeton, NJ, 1978).
6. D. H. Hathaway *et al.*, *Geophys. Astrophys. Fluid Dyn.* **13**, 287 (1979); D. H. Hathaway *et al.*, *ibid.* **15**, 7 (1980).
7. F. H. Busse, *J. Fluid Mech.* **72**, 67 (1975).
8. R. Krishnamurti, *J. Atmos. Sci.* **32**, 1353 (1975).
9. H. P. Greenspan, *The Theory of Rotating Fluids* (Cambridge Univ. Press, Cambridge, 1968).
10. F. H. Busse, *J. Fluid Mech.* **44**, 441 (1970); *Astrophys. J.* **159**, 629 (1970); *Astron. Astrophys.* **28**, 27 (1973); B. R. Durney, *Astrophys. J.* **161**, 1115 (1970); P. A. Gilman, *J. Atmos. Sci.* **32**, 1331 (1975).
11. F. H. Busse and P. G. Cuong, *Geophys. Astrophys. Fluid Dyn.* **8**, 17 (1977).
12. G. A. Glatzmaier, *J. Comput. Phys.* **55**, 461 (1984).
13. P. A. Gilman, *Geophys. Astrophys. Fluid Dyn.* **11**, 181 (1978). For the same values of Rayleigh, Taylor, and Prandtl numbers, no-slip boundaries for convection in a spherical shell reduce the induced differential rotation kinetic energy by a factor of about 25, compared to the stress-free boundary case [see (15)].
14. P. A. Gilman, *J. Fluid Mech.* **57**, 381 (1973). Although this calculation is for a thin annulus in Cartesian geometry rather than a spherical shell, it shows that the induced differential rotation kinetic energy for $P_r = 8$ is reduced, relative to the convection kinetic energy that drives it, by about a factor of 8 when compared to the case for $P_r = 1$ (approximately a linear relation in this Prandtl number range).
15. P. A. Gilman, *Geophys. Astrophys. Fluid Dyn.* **8**, 93 (1977).
16. Detailed analysis of the laboratory flows and their numerical simulations will be reported elsewhere (J. E. Hart, G. A. Glatzmaier, J. Toomre, *J. Fluid Mech.*, in press).
17. This research was supported in part by the National Aeronautics and Space Administration through contract NAS-8-31958 to the University of Colorado. The National Center for Atmospheric Research is sponsored by the National Science Foundation. We thank B. Fiedler, E. Graham, D. Hathaway, R. Malone, W. Merryfield, and J. Miller for substantial help with analysis and modeling during the development phases of this experiment. The engineering and fabrication of the instrument was guided by R. Kroger of Aerojet ElectroSystems Company, and additional technical support was provided by Marshall Space Flight Center.

3 April 1986; accepted 1 July 1986